

Observation of novel topological states in hyperbolic lattices

Weixuan Zhang^{1*}, Hao Yuan^{1*}, Na Sun¹, Houjun Sun², and Xiangdong Zhang^{1§}

¹Key Laboratory of advanced optoelectronic quantum architecture and measurements of Ministry of Education, Beijing Key Laboratory of Nanophotonics & Ultrafine Optoelectronic Systems, School of Physics, Beijing Institute of Technology, 100081, Beijing, China

²Beijing Key Laboratory of Millimeter wave and Terahertz Techniques, School of Information and Electronics, Beijing Institute of Technology, Beijing 100081, China

*These authors contributed equally to this work. [§]Author to whom any correspondence should be addressed. E-mail: zhangxd@bit.edu.cn

The discovery of novel topological states has served as a major branch in physics and material science. However, to date, most of the established topological states of matter have been employed in Euclidean systems, where the interplay between unique geometrical characteristics of curved spaces and exotic topological phases is less explored, especially on the experimental perspective. Recently, the experimental realization of the hyperbolic lattice, which is the regular tessellation in non-Euclidean spaces with a constant negative curvature, has attracted much attention in the field of simulating exotic phenomena from quantum physics in curved spaces to the general relativity. The question is whether there are novel topological states in such a non-Euclidean system without analogues in Euclidean spaces. Here, we demonstrate both in theory and experiment that novel topological states possessing unique properties compared with their Euclidean counterparts can exist in engineered hyperbolic lattices. Specially, based on the extended Haldane model, the boundary-dominated first-order Chern edge state with a nontrivial real-space Chern number is achieved, and the associated one-way propagation is proven. Furthermore, we show that fractal-like midgap higher-order zero modes appear in deformed hyperbolic lattices, where the number of zero modes increases exponentially with the increase of lattice size. These novel topological states are observed in designed hyperbolic circuit networks by measuring site-resolved impedance responses and dynamics of voltage packets. Our findings suggest a novel platform to study topological phases beyond Euclidean space and may have potential applications in the field of designing high-efficient topological devices, such as topological lasers, with extremely fewer trivial regions.

Exploring novel topological phases of matter is one of the most fascinating reach areas in physics¹⁻⁶. Since the pioneering discovery of the integer quantum Hall effect in 1980⁸, a large number of fascinating quantum phases with distinct topological properties have been successively proposed. These novel topological states have been revealed in various systems possessing completely different characteristics, ranging from lower dimensions to higher dimensions⁹⁻¹¹, from Hermitian systems to non-Hermitian systems¹²⁻¹⁴, from periodic structures to disordered structures¹⁵, from single-particle systems to many-particle systems^{16,17}, from linear lattices to nonlinear lattices¹⁸⁻²⁰, from static systems to dynamic systems^{21, 22}, and so on. To date, most of the established topological states of matter have been principally employed in Euclidean geometry with a zero curvature.

On the other hand, the non-Euclidean geometry exists widely in nature and plays important roles in many different fields, including mathematics, the holographic principle, the general theory of relativity and so on. To experimentally explore the novel physics of curved spaces, the controllable laboratory setups are required to be constructed. Recently, using circuit quantum electrodynamics, the experimental realization of discrete hyperbolic lattices⁷, which are regular tessellations in curved spaces with constant negative curvature, has stimulated many advances in non-Euclidean geometry and hyperbolic physics, such as the Bloch band theory of hyperbolic lattices^{23, 24}, crystallography of hyperbolic lattices²⁵, quantum field theories in continuous negatively curved space²⁶, hyperbolic drum in circuit networks²⁷ and so on²⁸⁻³¹. Additionally, it is worthwhile to note that boundary sites always occupy a finite portion of the total site regardless of the size for the hyperbolic lattice due to the negative curvature. This is completely contrary to the case of Euclidean lattices, where the ratio between the number of boundary sites to the total sites approaches to zero in the thermodynamic limit. In this case, inspired by the fascinating phenomena revealed in hyperbolic lattices and the associated distinct boundary geometry, it is important to ask whether there are undiscovered topological states in hyperbolic lattices without counterparts in Euclidean space³², and how to construct the hyperbolic topological phases in experiments.

In this work, we report the first experimental observation of two kinds of novel topological states, that are boundary-dominated first-order Chern edge states and fractal-like higher-order zero modes, in engineered hyperbolic lattices. In particular, by extending the original Haldane model in Euclidean space to hyperbolic lattices, unidirectional edge states with nontrivial real-space Chern numbers are proposed. Moreover, based on the deformed hyperbolic lattice with unequal coupling strengths in different layers, fractal-like midgap higher-order corner modes are revealed. In experiments, these novel topological states are observed based on the designed hyperbolic circuit networks. Our finding unfolds the intriguing properties of hyperbolic topological states and suggests

a new route to design highly compact topological devices with efficient spatial utilization.

Boundary-dominated first-order topological states in hyperbolic Chern insulators. We start by briefly introducing the projection scheme of a hyperbolic plane with a uniform negative curvature in the (2+1)-dimensional Minkowski space onto a complex unit disk. As illustrated in Fig. 1a, under the stereographic projection with the reference point located at $(x=0, y=0, t=-1)$, a hyperboloid defined by $t^2 - x^2 - y^2 = 1$ could be mapped to a unit disk at $t=0$, where the geodesics on the hyperboloid are projected to circular arcs perpendicular to boundaries of the disk (green lines). Such a unit disk is called the Poincaré disk equipped with the hyperbolic metric. Based on this projection scheme, the hyperbolic lattice, which is a discrete tessellation of the two-dimensional hyperbolic space, could be mapped to the Poincaré disk.

To illustrate the hyperbolic lattice in the Poincaré disk, we introduce the Schläfli notation $\{p, q\}$, which represents a tessellation of the plane by p -sided regular polygons with the coordination number q , to label the lattice pattern. We note that only the triangular lattice $\{3, 6\}$, square lattice $\{4, 4\}$, and honeycomb lattice $\{6, 3\}$ could exist in the two-dimensional (2D) Euclidean space, where the relationship of $(p-2)(q-2)=4$ must be satisfied. In contrast, the hyperbolic tessellation is ensured by $(p-2)(q-2)>4$ so that there are infinite kinds of lattice models in the hyperbolic space⁷. Here, we focus on the hexagonal hyperbolic lattice $\{6, 4\}$ embedded into the Poincaré disk, as presented in Fig. 1b, where all neighboring lattice sites possess equal hyperbolic distances. More details about the geometric properties and mathematical representations of the hyperbolic lattice are provided in Supplementary Note 1.

To construct topological states in the hyperbolic lattice, we extend the Haldane model³³ originally defined in Euclidean space to the hyperbolic lattice $\{6, 4\}$. The finite hyperbolic lattice $\{6, 4\}$ with a sixfold rotation invariance is topologically equivalent to successive quasi-concentric rings with L labeling the number of layers. The graph with $L=4$ is displayed in Fig. 1c, which corresponds to the hyperbolic lattice plotted in Poincaré disk in Fig. 1b. For clarity, we mark lattice sites in the first, second, third and fourth layers by cyan, blue, green and red dots, respectively. By introducing nearest-neighbor (NN) hoppings (γ) and direction-dependent next-nearest-neighbor (NNN) hoppings ($\lambda e^{i\varphi}$) in each hexagon, the hyperbolic Haldane model is achieved. Detailed coupling patterns in hexagons composed of lattice sites from different layers are illustrated in the right insets of Fig. 1c, where solid lines and dashed arrow lines correspond to NN hoppings and NNN hoppings, respectively. In this case, the hyperbolic Haldane model can be effectively

described by a tight-binding Hamiltonian as:

$$H = \sum_{\langle i,j \rangle} \gamma a_i^\dagger a_j + \sum_{\langle\langle i,j \rangle\rangle} \lambda e^{i\varphi} a_i^\dagger a_j + h.c. \quad (1)$$

with $a_i^\dagger(a_i)$ being the creation (annihilation) operator at site i . The bracket $\langle \dots \rangle$ ($\langle\langle \dots \rangle\rangle$) indicates that the summation is restricted within NN (NNN) sites. φ is the geometrical phase of NNN couplings. Compared with the Haldane model defined in Euclidean space, where each bulk site possesses three NN couplings and six NNN couplings, there are four NN couplings and eight NNN couplings for the bulk site of the hyperbolic Haldane model.

Firstly, we perform a direct diagonalization of the Hamiltonian for the finite hyperbolic Haldane lattice with $\gamma=1$, $\lambda=0.2$, $\varphi=2\pi/3$ and $L=4$. Fig. 1d shows the calculated energy-spectrum of all eigenstates marked by n . To quantify the localization degree of associated eigenmodes on the boundary (the outermost layer), a quantity $V(\varepsilon) = \sum_{i \in L=4} |\varphi_i(\varepsilon)|^2 / \sum_{i \in L=1,2,3,4} |\varphi_i(\varepsilon)|^2$ is calculated for each eigenstate, where $\varphi_i(\varepsilon)$ is the complex amplitude at site i with eigen-energy being ε . It is noted that the value of $V(\varepsilon)$ approaches to 1 for the edge-concentrated eigenstate, while bulk-localized eigenmodes have a near-zero value of $V(\varepsilon)$. We find that edge states are mainly located around the zero-energy region, and bulk modes exist at the low- and high-energy ranges. To further illustrate the distribution of associated eigenmodes, we plot spatial profiles of bulk and edge eigenmodes with eigen-energies being $\varepsilon=-3.445$ ($n=5$) and $\varepsilon=0.1406$ ($n=230$) in Fig. 1e. It is clearly shown that the eigenmode at $\varepsilon=0.1406$ possesses the feature with significant edge localization, which is a key property of nontrivial topological states.

To further verify that the edge state is indeed topological, the Chern number should be calculated to characterize the system. However, since our proposed hyperbolic Haldane model is nonperiodic, the Chern number is undefined in the Brillouin zone torus. In this case, as shown in Fig. 1f, we calculate the real-space Chern number at each eigenenergy defined by³⁴

$$C = 12\pi i \sum_{j \in I} \sum_{k \in II} \sum_{l \in III} (P_{jk} P_{kl} P_{lj} - P_{jl} P_{lk} P_{kj}) \quad (2)$$

where j , k , and l are site indices in three regions I , II and III that are arranged anti-clockwise, as shown in the inset of Fig. 1f. The square of projection operator element $|P_{ij}|^2$ measures the correlation of the state density at two sites (i and j) when all states below the target energy are occupied. It is clearly shown that the real-space Chern number around the zero energy possesses a nontrivial value. While, due the finite size effect, the absolute value of calculated real-space Chern number is smaller than 1. The detailed method for the calculation of the real-space Chern number and numerical results with different lattice sizes are provided in Supplementary Note 2. We note that the nontrivial real-space Chern number clearly manifests the topological property of edge-localized eigenmodes

around the zero energy.

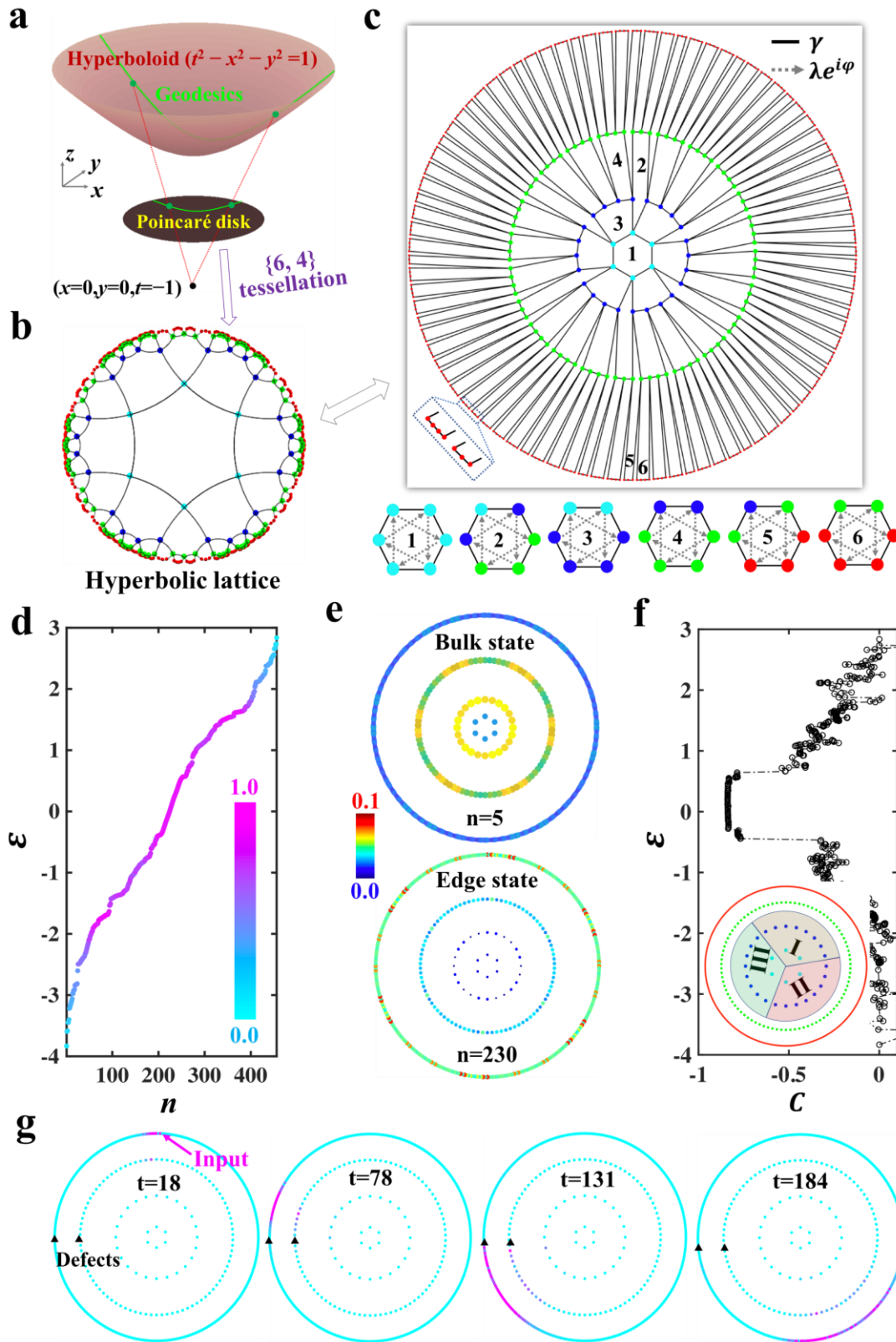


Figure 1. Hyperbolic Haldane model and boundary-dominated first-order topological edge states.

a. The left chart illustrates the stereographic projection scheme of a hyperbolic plane ($t^2 - x^2 - y^2 = 1$) onto the Poincaré disk at $t=0$. Green lines represent the geodesics on the hyperboloid, which are

projected to circular arcs perpendicular to boundaries of the Poincaré disk. **b.** The hyperbolic lattice $\{6, 4\}$ embedded into the Poincaré disk. **c.** The finite hyperbolic lattice $\{6, 4\}$ in the form of successive quasi-concentric rings with $L=4$ layers. The left-bottom inset displays the enlarged view of the outermost layer. Right insets plot coupling patterns in hexagons composed of lattice sites from different layers. **d.** The calculated eigen-spectrum of the system with $L=4$. The colormap corresponds to the quantity $V(\varepsilon)$ for the localization degree at the boundary. **e.** Profiles of bulk and edge states with eigen-energies of -3.445 and 0.1406 . **f.** The calculated real-space Chern number of each eigenmode. The inset plots three different regions I, II and III used in the calculation. **g.** Four charts present the spatial distributions of $|\varphi_i(t)|$ at different times with $t=18, 78, 131$ and 184 , respectively.

In addition, it is widely known that one-way edge states, which are robust against defects, should exist in the energy region with nontrivial real-space Chern numbers. Thus, by solving coupled model equations (see Supplementary Note 3), we numerically study the robust evolution of edge states by launching a wave packet $\psi_{\text{in}}(t)=\exp(-(t-t_0)^2/64)\sin(\varepsilon_c t)$ into an edge site as illustrated by the pink arrow in Fig. 1g, where several defects (marked by black triangles) with the extra onsite potential ($P_d=5$) exist at the outermost ring. Other parameters are set as $t_0=20$ and $\varepsilon_c=0.1$. Fig. 1g shows the spatial distributions of $|\varphi_i(t)|$ at different times with $t=18, 78, 131$ and 184 , respectively. It is clearly shown that the wave packet unidirectionally moves along edges of hyperbolic Chern insulator and passes through defects without backscattering. Additionally, during propagation, the wave packet is confined to the boundary and does not penetrate into the bulk. These numerical results further prove the existence of unidirectional edge states in the hyperbolic Haldane model. In Supplementary Note 4, numerical results of hyperbolic Chern insulators with different lattice sizes are provided, where all results are consistent with our claim on the existence of boundary-dominated topological states in the hyperbolic Haldane model. It is worthwhile to note that the ratio of the one-way topological channel composed of boundary sites to bulk sites in the hyperbolic Chern insulator is more than 0.9, which is much larger than the Euclidean counterpart. Hence, such a novel topological state is very beneficial for the realization of highly compact topological devices with an extremely less trivial region in the bulk.

Motivated by recent experimental breakthroughs in realizing various quantum phases by circuit networks³⁵⁻⁴¹, in the following, we design hyperbolic Chern circuits to observe above proposed novel topological states. Fig. 2a illustrates the photograph image of the fabricated circuit sample with $L=3$. The front and back sides of enlarged views (the pink dash block) and the schematic diagram of NN and NNN couplings are plotted in right insets. Specifically, three circuit nodes

connected by the capacitor C are considered to form an effective lattice site of the hyperbolic Chern insulator, as enclosed by the green block. Voltages at these three nodes are defined by $V_{i,1}$, $V_{i,2}$ and $V_{i,3}$, which could be suitably formulated to construct a pair of pseudospins ($V_{\uparrow i,i} = V_{i,1} + V_{i,2}e^{\pm i2\pi/3} + V_{i,3}e^{\mp i2\pi/3}$) for realizing required site couplings. To simulate the real-valued NN hopping rate, three capacitors (C_γ) framed by the red frame are used to directly link adjacent nodes without a cross. For the realization of NNN hopping rate with a direction-dependent phase ($e^{\pm i2\pi/3}$), three pairs of adjacent nodes are connected crossly via three capacitors C_λ enclosed by the blue block. Each node is grounded by an inductor L_g framed by the white block in the back side. The defect in the outermost ring is achieved by adding an extra grounding capacitor C_p . Additionally, boundary nodes should be additionally grounded by suitable capacitors to ensure the same resonance frequency as bulk nodes.

Through the appropriate setting of grounding and connecting, the circuit eigenequation is identical with that of the hyperbolic Chern insulator. Details for the derivation of circuit eigenequations are provided in Supplementary Note 5. In particular, the probability amplitude at the lattice site i is mapped to the voltage of pseudospin $V_{i,i}$. Amplitudes of the effective NN and NNN couplings equal to $\gamma = C_\gamma/C$ and $\lambda = C_\lambda/C$. The eigenenergy of the hyperbolic Haldane model is directly related to the eigenfrequency of the circuit network as $\varepsilon = f_0^2/f^2 - 3 - 4C_\gamma/C - 8C_\lambda/C$ with $f_0 = (2\pi\sqrt{CL_g})^{-1}$. It is noted that the tolerance of circuit elements is only 1% to avoid the detuning of circuit responses, and circuit parameters are set as $C=1$ nF, $C_\gamma=1$ nF, $C_\lambda=0.2$ nF, $L_g=1$ uH and $C_p=5$ nF. Details of the sample fabrication are provided in the Methods.

To analyze topological properties of the hyperbolic Chern circuit, we firstly measure the impedance responses of a bulk node (the black line) and an edge node (the red line) using the Wayne Kerr precision impedance analyzer, as plotted in Fig. 2b. It is shown that there are significant impedance peaks of the edge node but neglectable impedances of the bulk node in the frequency range from 1.67 MHz to 1.75 MHz (the red region), which matches the eigenenergy possessing nontrivial edge states. Fig. 2c presents simulation results of frequency-dependent impedance responses using the LTSPICE software. A good consistence between simulations and experiments is obtained, and the larger width of measured impedance peaks results from the lossy effect in the fabricated circuit. In addition, the spatial impedance distribution of the circuit at 1.708 MHz is further measured, as shown in Fig. 2d. We can see that the edge-concentrated impedance profile (similar to Fig. 1e with $n=230$) clearly proves the excitation of hyperbolic edge states.

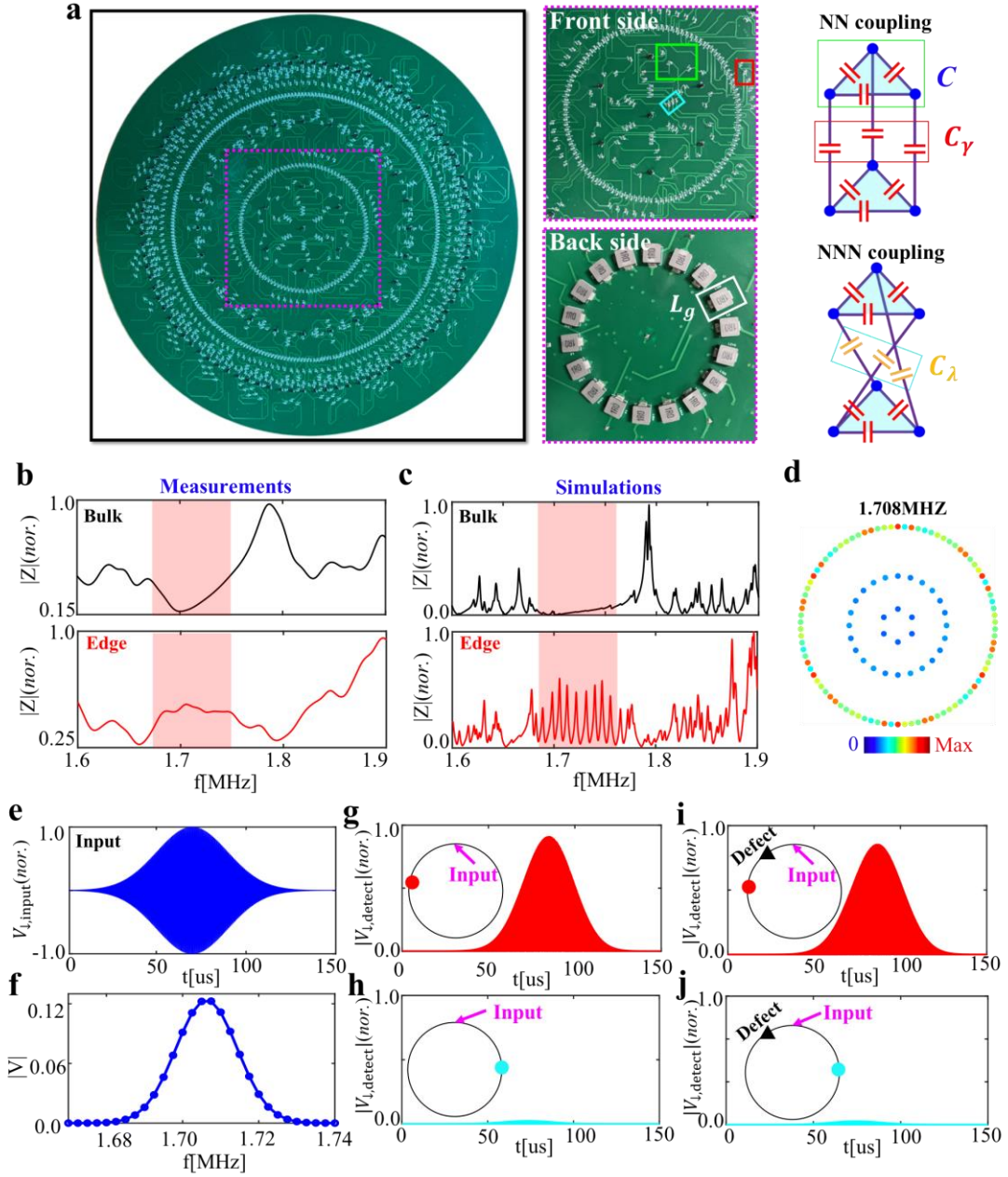


Figure 2. Observation of boundary-dominated topological states in the hyperbolic Chern circuit.

a. Photograph image of the fabricated hyperbolic circuit. The part of enlarged view and the equivalent schematic diagram are presented in right insets. **b and c.** Measured and simulated impedance responses of bulk and edge nodes. **d.** The measured impedance distributions at 1.708MHz. **e and f.** The voltage packet and the associated frequency spectrum of the injected voltage packet. **g and h.** The measured time tracks of the voltage pseudospin at nodes in the defect-free circuit along the counterclockwise and clockwise directions with respect to the excitation node. **i and j.** The measured time tracks of the voltage pseudospin at nodes in the circuit with a defect along the counterclockwise and clockwise directions with respect to the excitation node. Red and blue dots in insets mark the position of two detection nodes and the pink arrow presents the input node. The black triangle corresponds to the defect. The circuit

parameters used in experiments are set as $C=1$ nF, $C_\gamma=1$ nF, $C_\lambda=0.2$ nF, $L_g=1$ uH and $C_p=5$ nF.

Then, we measure the temporal dynamics of an effective voltage packet propagating in the hyperbolic Chern circuit. To ensure the excitation of voltage pseudospin, three voltage packets, which are expressed as $[V_{i,1}, V_{i,2}, V_{i,3}] = V(t)[1, \exp(i\frac{2\pi}{3}), \exp(-i\frac{2\pi}{3})]$ with $V(t) = V_0 \exp(-(t - t_0)^2/t_d^2) \sin(2\pi f_c t)$, are used. Details of the experimental technologies are provided in the Methods. Here, the time delay, packet width and central frequency of the voltage packet are set as $t_0=70$ μ s, $t_d=28$ μ s and $f_c=1.708$ MHz, respectively. The voltage packet and the associated frequency spectrum are shown in Fig. 2e and Fig. 2f. It is noted that the main components of the frequency spectrum are located in the range sustaining topological edge states, making only nontrivial edge states be excited. Fig. 2g and Fig. 2h present time tracks of the voltage packet in the defect-free circuit at two nodes, which are counterclockwise (the red dot) and clockwise (the cyan dot) to the excitation point (the pink arrow) with equal distances, respectively. It is clearly shown that only the counterclockwise circuit node possesses a significant response in the time-domain, indicating that the voltage packet propagates counterclockwise along the edge of hyperbolic Chern circuit. Then, we measure the voltage signal at these two nodes with the existence of a defect (the black triangle between the excitation node and the counterclockwise node), as shown in Fig. 2i and Fig. 2j. We can see that the magnitude of voltage packet at the counterclockwise node is nearly unchanged, indicating no significant backscattering appears when the voltage signal passes through the defect. Such a defect-immune voltage propagation clearly manifests the robustness of edge states. The above measurements are also consistent with simulations (see Supplementary Note 6), which clearly manifest the observation of boundary-dominated topological states in hyperbolic Chern circuits.

Fractal-like higher-order zero modes in deformed hyperbolic lattices. In addition to the boundary-dominated first-order topological states induced by the interplay between the Chern-class topology and the hyperbolic geometry, in the following, we prove that exotic higher-order zero modes existed in the gapped edge states can also be constructed in the deformed hyperbolic lattice.

Different from hyperbolic Chen lattices, which possess the complex NNN couplings to break the time-reversal symmetry, here we introduce a pair of distinct coupling strengths (γ_1 and γ_2) in the deformed hyperbolic lattice to realize the higher-order zero modes. The general protocol of hyperbolic lattices for achieving higher-order zero modes is presented in Fig. 3a. Six insets present the detailed coupling patterns in hexagons composed of lattice sites from different layers. In particular, the intralayer coupling strength of the outermost and $2nd$ ($1st$ and $3rd$) layers equals to

γ_1 (γ_2), as marked by black (pink) lines. Moreover, the interlayer coupling strength between the n th and $(n-1)$ th layers ($n=4, 3, 2$) is identical to the intralayer coupling strength of the n th layer.

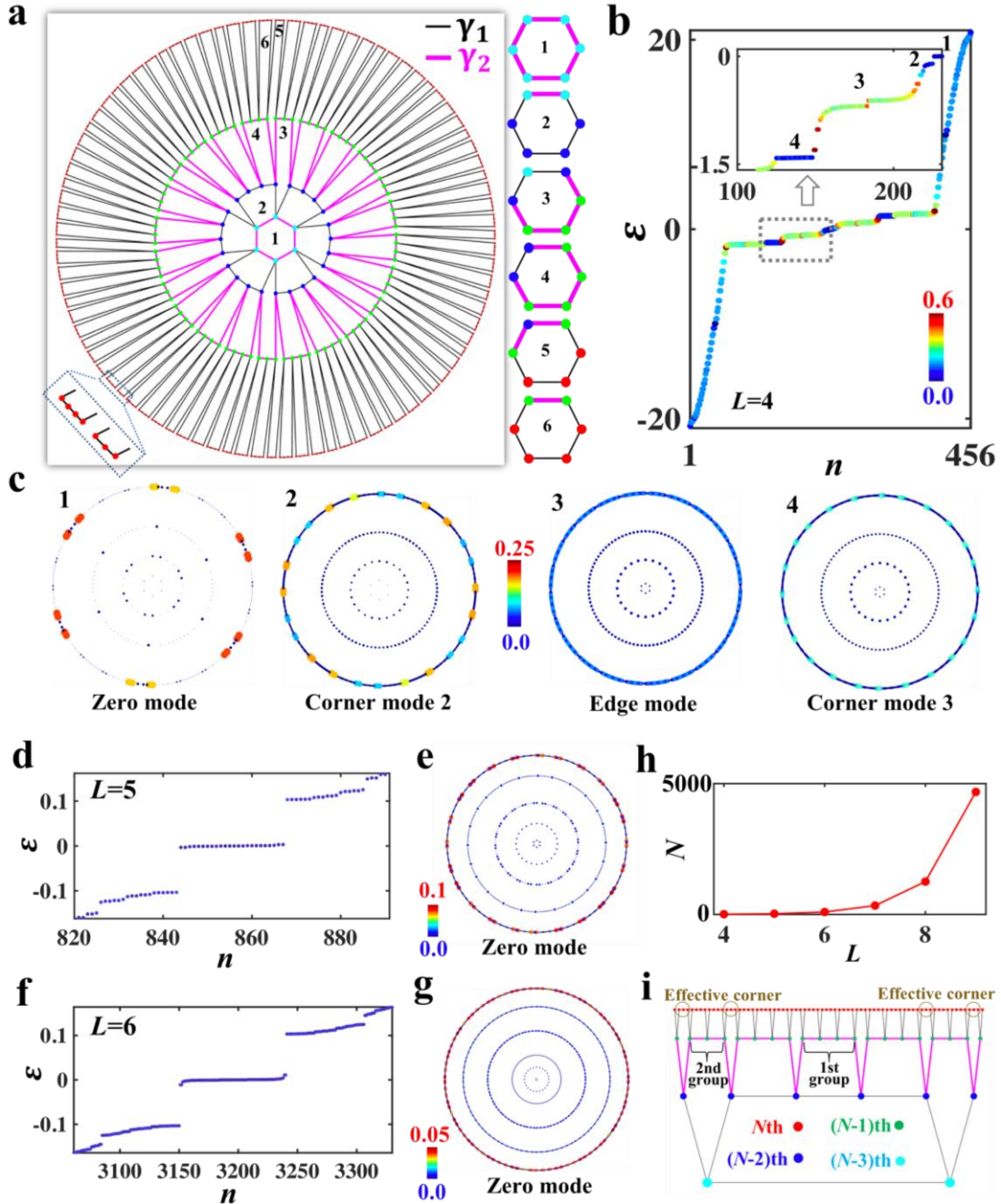


Figure 3. Fractal-like higher-order zero modes in the deformed hyperbolic lattice. **a.** The deformed hyperbolic lattice model for realizing fractal-like higher-order zero modes with $L=4$ layers. Right insets plot coupling patterns in hexagons composed of lattice sites from different layers. **b.** The calculated eigen-spectrum of the system with $L=4$. The colormap corresponds to the IPR of each eigenmode. The inset presents the enlarged spectrum with eigenenergies ranging from -1.5 to 0 . **c.** Profiles of the normalized density of states of eigenmodes in four different energy regions. **d** and **f.** The eigen-spectra of the hyperbolic lattice with $L=5$ and $L=6$, respectively. **e** and **g.** Density of states of zero modes with

$L=5$ and $L=6$, respectively. **h.** The relationship between the number of midgap zero modes and the layer number (L) of deformed hyperbolic lattices. **i.** Schematic diagram illustrating the effective corners in the outermost ring in the deformed hyperbolic lattice.

First, we numerically calculate the eigen-spectrum of the deformed hyperbolic lattice with coupling strengths being $\gamma_1 = 1$ and $\gamma_2 = 10$, as shown in Fig. 3b. The inset presents the enlarged eigen-spectrum ranging from -1.5 to 0. To quantify the localization degree of the associated eigenstate, the inverse participation ratio (*IPR*) of each eigenmode $IPR = \sum_i |\varphi_i(\varepsilon)|^{-4}$ is calculated, as presented by the color bar in Fig. 3b. It is noted that six zero-energy modes (marked by the number 1 in the inset) show the significant field-localization, which is manifested by the near-zero *IPR*. The *IPR*s of two other kinds of midgap eigenmodes around $\varepsilon = -0.1192$ and $\varepsilon = -1.41$ (marked by numbers 2 and 4 in the inset) also approach to zero, indicating the strong spatial localizations. In contrast, eigenmodes marked by the number 3 exhibit spatially extended features with larger values of *IPR*. To further illustrate the spatial distribution of each eigenstate, spatial profiles of density of state for these four types of eigenmodes are calculated, as plotted in Fig. 3c. It is clearly shown that the mode distribution of zero-energy eigenstates (labeled by the number 1 and called zero modes) is strongly localized around six 0D effective corners, which are unlike the real geometric corner in the form of intersections between 1D boundaries and are called as effective corners. In addition, spatial profiles of eigenmodes with energies being $\varepsilon \sim [-0.1348, -0.1021]$ (labeled by the number 2 and called ‘corner mode 2’) and $\varepsilon \sim [-1.415, -1.407]$ (labeled by the number 4 and called ‘corner mode 3’) also present the mode localization at twenty-four effective corners in the outermost ring. In contrast, the averaged spatial profile with $\varepsilon \sim [-0.6154, -0.2025]$ (labeled by the number 3) exhibits 1D edge localizations, where the eigen-field at corners is nearly zero. These numerical results clearly indicate that 0D corner-like eigenstates always appear in the gapped edge states.

It is worthwhile to note that these midgap higher-order zero modes in hyperbolic lattices possess similar characteristics to the filling anomaly induced 0D corner states in higher-order topological crystalline insulators⁴². In particular, identical symmetries, including the C_6 rotation, the time reversal, and chiral symmetries, are preserved in the deformed hyperbolic lattice as in C_6 -symmetric higher-order topological crystalline insulators. In this case, we infer that the nontrivial higher-order zero modes in the gapped edge states should result from obstructed atomic limits in deformed hyperbolic lattices. Numerical results for the system with larger intralayer couplings in the outermost ring ($\gamma_1 > \gamma_2$) are applied in Supplementary Note 7. In this case, similar to the trivial

atomic limit of C_6 -symmetric lattice models in Euclidean space, no midgap higher-order zero mode appears with larger intralayer coupling strengths around corners.

To illustrate the influence of size-dependent boundary geometries of hyperbolic lattices on the formation of higher-order zero modes, we further consider two larger systems with $L=5$ and $L=6$. Here, the intralayer coupling strength of the outermost ring ($\gamma_1=1$) is always smaller than that of the secondary outer ring ($\gamma_2=10$). In Figs. 3d and 3f, the eigen-spectra of deformed hyperbolic lattices with $L=5$ and $L=6$ are calculated. Interestingly, it is clearly shown that there are 24 and 90 midgap zero modes in hyperbolic lattices with $L=5$ and $L=6$. Furthermore, the associated spatial profiles of these zero modes are displayed in Figs. 3e and 3g. Similar to the case with $L=4$, we note that these zero modes are strongly localized around 24 (for $L=5$) and 90 (for $L=6$) corners in the outermost ring, exhibiting the same feature of 0D corner states in higher-order topological insulators. By further calculating the eigenspectral of deformed hyperbolic lattices with different numbers of layers, we could plot the relationship between the number of midgap zero modes (N) and the layer number (L) in Fig. 3h. It is shown that the numbers of zero modes increase exponentially with the increase of the layer number L . The size-dependent mode number is also satisfied for the corner mode 2 and the corner mode 3. It is worthwhile to note that such a phenomenon is similar to the higher-order topological corner states existing in quantum fractals⁴³, where the number of zero-energy modes depends on the generation number of fractal lattices.

To clarify the fractal-like higher-order zero modes in deformed hyperbolic lattices, the formation mechanism of effective corners in the outermost (the N th) ring should be illustrated. As shown in Fig. 3i, the lattice sites in the $(N-1)$ th ring (green dots) can be divided into two groups. The first (second) group is in the form of the linked chain with four (three) sites. It is noted that the lattice sites in the N th layer, which form hexagons combined with lattice sites of the second group in the $(N-1)$ th layer, could act as effective corners of zero modes, as enclosed by circles in earth-yellow. In addition, we note that the number of the second group in the $(N-1)$ th layer equals to the total number of lattice sites in the $(N-3)$ th layer, which increases exponentially with the increase of L . In this case, the number of effective corners in the outermost layer of zero modes can also exhibit an exponentially growing tendency with L , leading to the appearance of fractal-like higher-order zero modes in the deformed hyperbolic lattice.

Similar to the hyperbolic Chern insulator, we can also design circuit networks to observe higher-order zero modes. Fig. 4a illustrates the photograph image of the fabricated circuit with $L=4$, and the enlarged views of front and back sides of the sample (marked by the red dash block) are plotted in right insets. In particular, the coupling strength of γ_1 (γ_2) in the hyperbolic lattice model

is realized by linking circuit nodes through the capacitor C_1 (C_2), as framed by the blue (green) circle. And, each circuit node is grounded by an inductor L_{gc} enclosed by the white block. Moreover, boundary sites should be additionally grounded by two capacitors C_2 to ensure the same resonance frequency as bulk nodes. In this case, the circuit eigenequation is identical with that of the deformed hyperbolic lattice (see Supplementary Note 8 for details), and the eigenenergy of the hyperbolic lattice is directly related to the eigenfrequency of the circuit as $\varepsilon = f_c^2/f^2 - 2 - 2C_1/C_2$ with $f_c = 1/2\pi\sqrt{C_2L_{gc}}$. Here, circuit parameters are set as $C_1=1$ nF, $C_2=10$ nF and $L_{gc}=3.3$ uH, and the tolerance of those circuit elements is limited by 1%.

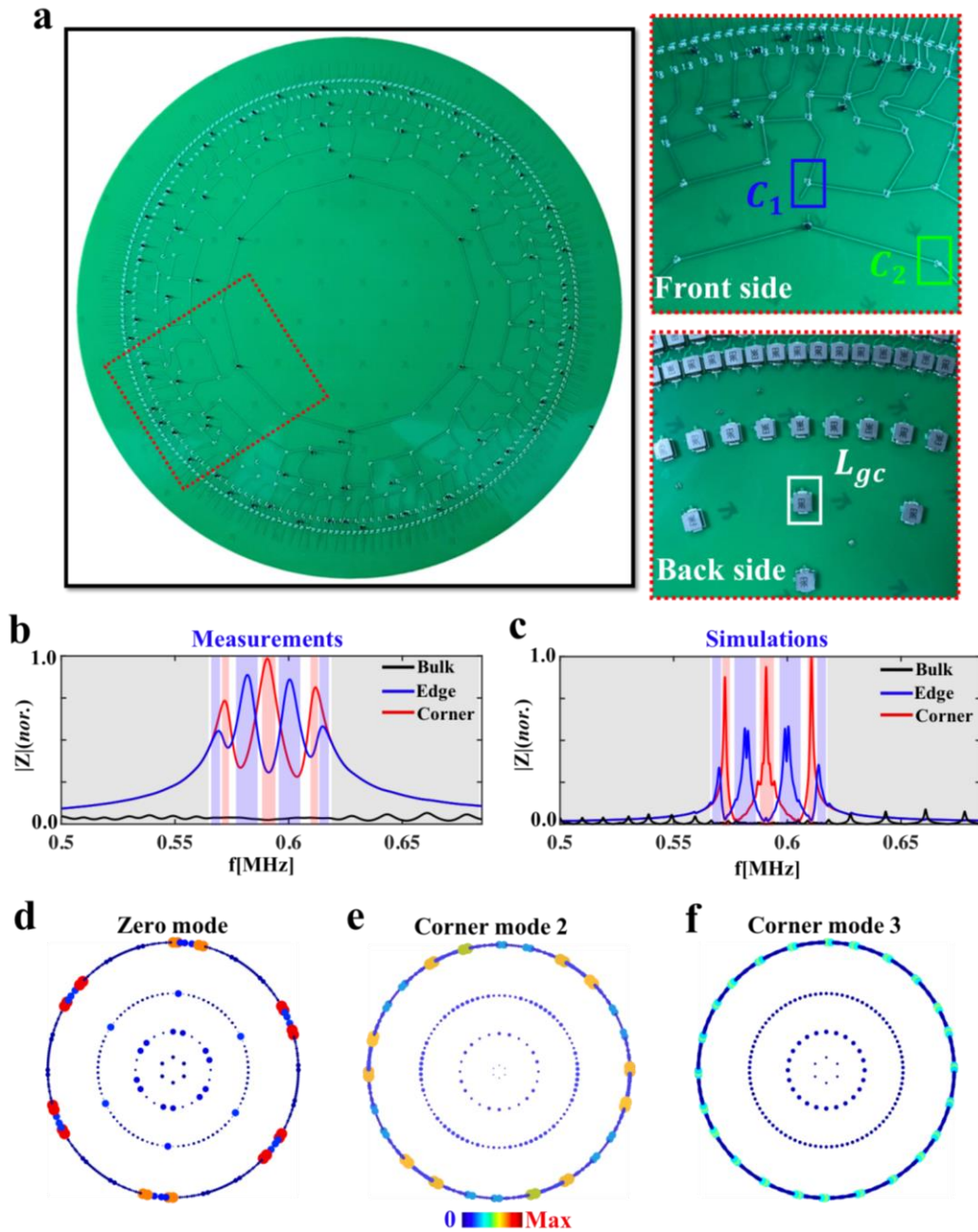


Figure 4. Observation of higher-order zero modes in the hyperbolic circuit. a. Photograph image of

the fabricated hyperbolic circuit. Right insets display the enlarged view of the sample as well as the associated schematic diagram. **b and c.** Measured and simulated impedance responses of selected bulk, edge and corner nodes. **d-f.** The profiles of higher-order zero modes and other two 0D corner states of the recovered circuit Laplacian. Circuit parameters used in experiments are set as $C_1=1$ nF, $C_2=10$ nF, and $L_{gc}=3.3$ uH.

To observe higher-order corner modes, we measure site-resolved impedance responses of selected bulk, edge and corner nodes, as shown in Fig. 4b. The corresponding numerical results are presented in Fig. 4c, where measured results are consistent with simulations and wider peaks in experiments result from lossy effects in the sample. It is clearly shown that the corner node possesses significant impedance peaks in three frequency ranges marked by red regions. In particular, the frequency of the impedance peak in the central red region (around 0.591MHz) matches to the zero-energy of the hyperbolic lattice model, that corresponds to the excitation of higher-order zero mode. It is worthy to note that due to the extremely small spectrum distance between zero modes and ‘corner mode 2’, the impedance peaks induced by these two kinds of corner states are merged together. Additionally, other two peaks of the corner node are originated from the resonance of ‘corner mode 3’ with positive and negative energies. Additionally, measured impedances of bulk and edge nodes are relatively small in frequency regions sustaining corner impedance peaks, indicating the corner modes exist in the bandgaps of bulk and edge states. The edge node shows large impedance peaks in four frequency regions marked by blue regions, which are consistent with the calculated eigen-energies of edge states in Fig. 3b (and the chiral symmetric counterpart with positive energies). The bulk node possesses many little impedance peaks in low-frequency and high-frequency regions shown in black regions, corresponding to resonance peaks associated to bulk modes.

To obtain the spatial distribution of higher-order 0D corner modes, we further recover the circuit admittance spectrum (see Method for details), and illustrate the spatial distributions of three different higher-order 0D corner modes of the recovered circuit Laplacian, as shown in Figs. 4d-4f. We can see that the recovered mode distributions are consistent with spatial profiles of higher-order corner modes in Fig. 3c. These experimental results clearly prove that hyperbolic higher-order corner modes have been fulfilled in our designed circuit network.

Discussion and Conclusion. We report the first experimental observation of boundary-dominated first-order Chern edge states and fractal-like higher-order zero modes in hyperbolic circuit networks.

By extending the definition of the Haldane model to hyperbolic spaces, a unidirectional edge state with nontrivial real-space Chern numbers is proposed. Besides the first-order topological state, the fractal-like midgap higher-order zero modes are also revealed based on the deformed hyperbolic lattice with unequal coupling strengths in different layers. The physical origin for the appearance of these exotic topological states results from the negative curvature induced boundary effect, where boundary sites always occupy a finite portion of the total site regardless of the system size. These fascinating topological states are observed in experiments by hyperbolic circuit networks. Compared with topological states in Euclidean space, one significant feature of the hyperbolic counterpart is that the edge lattice sites acting as the topological channel occupy a large ratio of total lattice sites even at the thermodynamic limit. Hence, by incorporating the proposed hyperbolic topological states into the design of robust functional devices in other classical wave systems, such as topological lasers, the operational efficiency and spatial utilization may be remarkably improved. Our proposal provides a flexible platform to further investigate and visualize more interesting phenomena related to topological physics in hyperbolic lattices.

With the flexibility that the connection and grounding of circuit nodes are allowed in any desired way free from constraints of locality and dimensionality, the high-dimensional topological hyperbolic lattice with non-local site couplings could also be achieved. Moreover, including nonreciprocal, non-Hermitian and non-linear elements in the circuit network, the novel behavior induced by the interplay between the non-Hermitian, non-linear, topology and curvature can be investigated in experiments. Finally, the designed circuit simulator could also give a new way to manipulate the electronic signals with exotic behaviors.

Methods.

Sample fabrications and circuit measurements. We exploit electric circuits by using LCEDA program software, where the PCB composition, stack-up layout, internal layer and grounding design are suitably engineered. Here, the PCBs possessing the Chern edge states and higher-order zero modes have six and four layers, respectively, where two layers are used for the inner electric layer and the node couplings are arranged in the remained layers. It is worth noting that the all grounded components are grounded through blind buried holes. Moreover, all PCB traces have a relatively large width (0.75 mm) to reduce the parasitic inductance, and the spacing between electronic devices is also large enough to avert spurious inductive coupling. The SMP connectors are welded on the PCB nodes for the signal input. To ensure the tolerance of circuit elements and series resistance of inductors to be as low as possible, we use a WK6500B impedance analyzer to select circuit elements

with high accuracy (the disorder strength is only 1%) and low losses.

For the time-domain measurement, we use two signal generators (DG5072) to inject three designed wave packets with required initial phases for exciting the voltage pseudospin. One output of the signal generator (the initial phase is set to 0) is directly connected to one end of the oscilloscope (Agilent Technologies Infiniivision DSO7104B) to ensure an accurate start time. The scanning speed of oscilloscope is set as 10ms/s. The measured voltage signals are in the range from 0 μ s to 200 μ s in the time domain, where 0 μ s is defined as the time for the simultaneous signal injection and measurement.

Recovering the circuit admittance spectrum involves a series of operations, where a current is injected at each circuit node individually and the voltages at all circuit nodes are measured at the same time. Based on the measured voltages and input currents, we can obtain Green's function of the hyperbolic circuit, which is the inverse of the circuit Laplacian. Calculating the eigenvalues and eigenvectors of the recovered circuit Laplacian, the admittance eigen-spectrum and the associated mode profiles are obtained.

Reference

1. Hasan, M. Z. & Kane, C. L. Colloquium: Topological insulators. *Rev. Mod. Phys.* **82**, 3045–3067 (2010).
2. Qi, X.-L. & Zhang, S.-C. Topological insulators and superconductors. *Rev. Mod. Phys.* **83**, 1057–1110 (2011).
3. Lu, L., Joannopoulos, J. D. & Soljačić, M. Topological photonics. *Nat. Photonics* **8**, 821-829 (2014).
4. Armitage, N. P., Mele, E. J. & Vishwanath, A. Weyl and Dirac semimetals in three-dimensional solids. *Rev. Mod. Phys.* **90**, 015001 (2018).
5. Ozawa, T., Price, H. M., Amo, A., Goldman, N., Hafezi, M., Lu, L., Rechtsman, M. C., Schuster, D., Zilberberg, O. & Carusotto, L. Topological photonics. *Rev. Mod. Phys.* **91**, 015006 (2019).
6. Ma, G., Meng, X. & Chan, C. T. Topological phases in acoustic and mechanical systems. *Nat. Rev. Phys.* **1**, 281-294 (2019).
7. Kollár, A. J., Fitzpatrick, M. & Houck, A. A. Hyperbolic lattices in circuit quantum electrodynamics. *Nature* **571**, 45 (2019).
8. Klitzing, K. v., Dorda, G. & Pepper, M. New method for high-accuracy determination of the

- fine-structure constant based on quantized hall resistance. *Phys. Rev. Lett.* **45**, 494–497 (1980).
9. Zhang, S.-C. & Hu, J. A four-dimensional generalization of the quantum hall effect. *Science* **294**, 823 (2001).
 10. Zilberberg, O., Huang, S., Guglielmon, J., Wang, M., Chen, K. P., Kraus, Y. E. & Rechtsman, M. C. Photonic topological boundary pumping as a probe of 4d quantum hall physics. *Nature* **553**, 59 (2018)..
 11. Lohse, M., Schweizer, C., Price, H. M., Zilberberg, O. & Bloch, I. Exploring 4d quantum hall physics with a 2d topological charge pump. *Nature* **553**, 55 (2018).
 12. Gong, Z. et al. Topological phases of non-Hermitian systems. *Phys. Rev. X* **8**, 031079 (2018).
 13. Yao, S. & Wang, Z. Edge states and topological invariants of non-Hermitian systems. *Phys. Rev. Lett.* **121**, 086803 (2018).
 14. Okuma, N., Kawabata, K., Shiozaki, K. & Sato, M. Topological origin of non-Hermitian skin effects. *Phys. Rev. Lett.* **124**, 086801 (2020).
 15. Li, J., Chu, R.-L., Jain, J. K. & Shen, S.-Q. Topological Anderson insulator. *Phys. Rev. Lett.* **102**, 136806 (2009).
 16. Sheng, D. N., Gu, Z.-C., Sun, K. & Sheng, L. Fractional quantum hall effect in the absence of landau levels. *Nat. Commun.* **2**, 389 (2011).
 17. Regnault, N. & Andrei Bernevig, B. Fractional Chern insulator. *Phys. Rev. X* **1**, 021014 (2011).
 18. Harari, G. et al. Topological insulator laser: theory. *Science* **359**, eaar4003 (2018).
 19. Bandres, M. A. et al. Topological insulator laser: experiments. *Science* **359**, eaar4005 (2018).
 20. Zhang, W., Xie, X., Hao, H. et al. Low-threshold topological nanolasers based on the second-order corner state. *Light Sci. Appl.* **9**, 109 (2020).
 21. Kitagawa, T., Berg, E., Rudner, M. & Demler, E. Topological characterization of periodically driven quantum systems. *Phys. Rev. B* **82**, 235114 (2010).
 22. Lindner, N. H., Refael, G. & Galitski, V. Floquet topological insulator in semiconductor quantum wells. *Nature Phys.* **7**, 490–495 (2011).
 23. Maciejko, J. & Rayan, S., Automorphic Bloch theorems for finite hyperbolic lattices. arXiv:2108.09314.
 24. Maciejko, J. & Rayan, S., Hyperbolic band theory. *Science Advances* **7**, eabe9170 (2021).
 25. Boettcher, I., Gorshkov, A. V., Kollár, A. J., Maciejko, J., Rayan, S. & Thomale, R., Crystallography of hyperbolic lattices. arXiv:2105.01087.
 26. Boettcher, I., Bienias, P., Belyansky, R., Kollár, A. J., & Gorshkov, A. V., Quantum

- simulation of hyperbolic space with circuit quantum electrodynamics: From graphs to geometry. *Phys. Rev. A* **102**, 032208 (2020).
27. Lenggenhager, P. M. et. al, Electric-circuit realization of a hyperbolic drum, arXiv:2109.01148 (2021).
28. Stegmaier, A., Upreti, L. K., Thomale, R., & Boettcher, I., Universality of Hofstadter butterflies on hyperbolic lattices, arXiv:2111.05779v1.
29. Boyle, L., Dickens, M. & Flicker, F., Conformal quasicrystals and holography. *Phys. Rev. X* **10**, 011009 (2020).
30. Kollár, A. J., Fitzpatrick, M., Sarnak, P. & Houck, A. A. Line-graph lattices: Euclidean and non-Euclidean flat bands, and implementations in circuit quantum electrodynamics. *Commun. Math. Phys.* **376**, 1909 (2019).
31. Zhang, R., Lv, C., Yan, Y., & Zhou, Q. Efimov-like states and quantum funneling effects on synthetic hyperbolic surfaces, *Science Bulletin.* **66**, 1967 (2021).
32. Yu, S., Piao, X. & Park, N. Topological hyperbolic lattices. *Phys. Rev. Lett.* **125**, 053901 (2020).
33. Haldane, F. D. M. Model for a quantum hall effect without landau levels: condensed-matter realization of the "Parity Anomaly". *Phys. Rev. Lett.* **61**, 2015 (1988).
34. Mitchell, N. P. et al. Amorphous topological insulators constructed from random point sets. *Nat. Phys.* **14**, 380–385 (2018).
35. Ning, J., Owens, C., Sommer, A., Schuster, D. & Simon, J. Time and site resolved dynamics in a topological circuit. *Phys. Rev. X* **5**, 021031 (2015).
36. Albert, V. V., Glazman, L. I. & Jiang, L. Topological properties of linear circuit lattices. *Phys. Rev. Lett.* **114**, 173902 (2015).
37. Lee, C., Imhof, S., Berger, C. et al. Topolectrical circuits. *Communications Physics* **1**, 39 (2018).
38. Imhof, S., Berger, C., Bayer, F., Brehm, J., Molenkamp, L. W., Kiessling, T., Schindler, F., Lee, C. H., Greiter, M., Neupert, T. & Thomale, R. Topolectrical-circuit realization of topological corner modes. *Nat. Phys.* **14**, 925 (2018).
39. Zhang, W., Zou, D., Pei, Q., He, W., Bao, J., Sun, H. & Zhang, X. Experimental observation of higher-order topological anderson insulators. *Phys. Rev. Lett.* **126**, 146802 (2021).
40. Olekhno, N., Kretev, E., Stepanenko, A., Filonov, D., Yaroshenko, V., Cappello, B., Matekovits, L. & Gorlach, M. A. Topological edge states of interacting photon pairs realized in a topolectrical circuit. *Nat. Commun.* **11**, 1436 (2020).

41. Wang, Y., Price, H. M., Zhang, B. & Chong, Y. D. Circuit realization of a four-dimensional topological insulator. *Nat. Commun.* **11**, 2356, (2020).
42. Benalcazar, W. A., Li, T. & Hughes, T. L. Quantization of fractional corner charge in Cn-symmetric higher-order topological crystalline insulators. *Phys. Rev. B* **99**, 245151 (2019).
43. Pai, S. & Prem, A. Topological states on fractal lattices. *Phys. Rev. B* **100**, 155135 (2019).

Acknowledgements

This work was supported by the National Key R & D Program of China under Grant No. 2017YFA0303800 and the National Natural Science Foundation of China (No. 91850205, No. 61421001 and No.12104041).